

# Rashba-induced spin texture and spin-layer-locking effects in the antiferromagnetic $\text{CrI}_3$ bilayer

Sukanya Ghosh<sup>\*\*</sup>, Nataša Stojić and Nadia Binggeli

*Abdus Salam International Centre for Theoretical Physics, Strada Costiera 11, 34151 Trieste, Italy*

## ARTICLE INFO

### Keywords:

Spin-layer locking  
Electric field  
First-principles calculations  
Reciprocal-space spin texture  
2D materials

## ABSTRACT

The antiferromagnetic (AFM)  $\text{CrI}_3$  bilayer is a particularly interesting representative of van der Waals 2D semiconductors, which are currently being studied for their magnetism and for their potential in spintronics. Using ab initio density-functional theory calculations, we investigate the spin texture in momentum space of the states of the (doubly degenerate) highest valence band of the AFM  $\text{CrI}_3$  bilayer with Cr-spin moments perpendicular to the layers. We find the existence, in the main central part of the Brillouin zone, of a Rashba in-plane spin texture of opposite signs on the two layers, resulting from the intrinsic local electric fields acting on each layer. To study the layer segregation of the wavefunctions, we apply a small electric field that splits the degenerate states according to their layer occupancy. We find that the wavefunctions of the highest valence band are layer-segregated, belonging to only one of the two layers with opposite in-plane spin textures, and the segregation occurs over nearly the whole Brillouin zone. The corresponding layer locking of the in-plane-canted spin is related to the separation in energy of the highest AFM band from the rest of the valence bands. We explain how the band interactions destroy the layer locking at the  $K$ ,  $K'$ , and  $\Gamma$  points. Furthermore, we compare the layer locking of the in-plane-canted spin in our AFM bilayer system with the hidden spin polarization in centrosymmetric nonmagnetic materials, pointing out the differences in segregation mechanisms and their consequences for the layer locking. We note that a similar Rashba effect with layer locking of in-plane-canted spin could occur in other van der Waals AFM bilayers with strong spin-orbit coupling and an isolated energy band.

## 1. Introduction

The recent discovery of intrinsic magnetic order in atomically thin semiconducting van der Waals crystals [1, 2] is opening avenues for fundamental research into 2D magnetism [3] and for the creation of low-power spintronic devices [4]. A particularly interesting material in this context is  $\text{CrI}_3$ , in its monolayer and bilayer forms. Monolayer  $\text{CrI}_3$  is ferromagnetic (FM) with an out-of-plane magnetization easy axis and a Curie temperature of 45 K [5]. In a bilayer, the weak van der Waals forces bind the two monolayers, whose intralayer couplings remain FM. The  $\text{CrI}_3$  bilayer is experimentally observed to be a layered antiferromagnet [2, 6, 7, 8, 5], with a Néel temperature similar to the monolayer's Curie temperature [8, 5].

In the last decade, antiferromagnets have become increasingly more appealing for spintronics, owing to their advantageous properties with respect to ferromagnets: antiferromagnetic (AFM) materials do not produce stray fields, permitting high-density memory integration, and are much less sensitive to magnetic field perturbations, providing the necessary stability for data storage [9, 10]. In addition, antiferromagnets have much faster spin dynamics than ferromagnets, which is necessary for ultrafast data processing [11].

The applications of the  $\text{CrI}_3$  bilayer are conceived on the basis of its layered AFM ground state and the ease of its transformation to the FM phase (low critical magnetic field of 0.6–0.7 T) [2]. The switching and tuning of the interlayer exchange from AFM to FM has been heavily investigated and obtained experimentally by various external perturbations [8, 5, 12, 13]. For example, the  $\text{CrI}_3$  bilayer and its multilayers are unique in their ability to simultaneously act as a tunneling barrier and a spin-filtering layer, thanks to their semiconducting nature and switchable magnetic state. Consequently, they display exceptional magnetoresistance properties upon the application of a magnetic field in both experimental studies [14, 15, 16] and theoretical studies [17, 18]. Recently, proximity spin-orbit torque on the  $\text{CrI}_3$  bilayer in a van der Waals heterostructure was shown theoretically [19]. At the same time, giant second-harmonic

<sup>\*</sup>Present affiliation: Department of Physics and Astronomy, Uppsala University, PO Box 516, SE-751 20 Uppsala, Sweden

<sup>\*</sup>email: sukanya.ghosh@physics.uu.se

ORCID(s):

generation was observed in the AFM  $\text{CrI}_3$  bilayer and was explained by the simultaneous absence of both inversion symmetry and time-reversal symmetry in its layered antiferromagnet structure [20], which are also found to activate and control Raman divergent optical selection rules [21]. The influence of symmetry operations for the magneto-optical Kerr effect was recently shown for AFM and FM  $\text{CrI}_3$ - $\text{CrBr}_3$  and  $\text{CrI}_3$  bilayers [22]. However, despite the great interest in the AFM ground state of the bilayer and newly discovered properties and phenomena stemming from its layered magnetic order, little is known about its  $\mathbf{k}$ -space spin texture. Spin texture can be of vital importance as it determines how spin-polarized currents can be manipulated for spintronic devices. It has been heavily investigated in nonmagnetic materials, especially after the discovery of hidden spin polarization [23, 24, 25, 26] and spin-layer locking [27, 28] in inversion-symmetric nonmagnetic semiconductors and semimetals. In contrast, the influence of the AFM order and the underlying symmetries on the spin texture in general is not well understood and is currently being studied in other systems, such as in the spin textures in hybrid organic–inorganic perovskites [29].

In this work, we study the  $\mathbf{k}$ -space spin texture of the  $\text{CrI}_3$  bilayer upper valence states by using density-functional theory. We find that the spin texture of the bilayer is essentially tangential and characterized by layer locking of the in-plane-canted spin. In addition, the Rashba effect is not accompanied by the typical energy splitting. To be able to evaluate the layer-dependent properties, we apply a small electric field that splits the AFM degenerate states according to their layer localization. We find that the wavefunctions of the two highest valence states are spatially segregated almost throughout the Brillouin zone (BZ) on one of the two layers featuring opposite in-plane spin textures. We point out that the wavefunction layer segregation is made possible by the AFM order and energy separation of the band. We show that the layer segregation is broken essentially only at the  $K$  and  $K'$  points and somewhat at the  $\Gamma$  point, which can be understood on the basis of the properties of monolayer band structure. We also compare the Rashba effect in the AFM bilayer with the hidden spin polarization in centrosymmetric nonmagnetic 2D materials.

## 2. System and computational method

Our calculations are performed using density-functional theory as implemented in the Quantum ESPRESSO package with the plane-wave basis set and pseudopotentials [30]. The local spin density approximation is used as the exchange-correlation functional to treat interactions between the electrons [31]. The coupling between electron spin and its orbital angular momentum is considered by our including the fully relativistic effect. The electron-ion interactions are described by the fully relativistic projector augmented wave pseudopotentials [32]. The plane-wave cutoffs for the kinetic energy and charge density for all our calculations are 60 Ry and 650 Ry, respectively. We use the  $\Gamma$ -centered Monkhorst-Pack  $k$ -point grid of  $24 \times 24 \times 1$ . The periodic images of the  $\text{CrI}_3$  bilayer are separated by a vacuum region with a thickness of 30 Å. In the structural relaxations, all coordinates are relaxed until the force on each atom becomes smaller than 0.1 mRy/bohr.

We concentrate on the  $\text{CrI}_3$  bilayer with monoclinic layer stacking and  $C_{2h}$  space-group symmetry. This is the common experimental form of the bilayer obtained by exfoliation from bulk  $\text{CrI}_3$  at room temperature, and which remains in that form when cooled to temperatures below the Néel temperature [20, 6]. The bilayer in that structure has been the focus of enormous attention because of its layered AFM ground state, which can be conveniently switched experimentally to the FM state (by a weak magnetic field as well as by electrical means) [2, 5, 8, 12].

Our optimized equilibrium local density approximation lattice constant for the  $\text{CrI}_3$  bilayer is 6.69 Å, and the innermost distance between the two layers is 3.36 Å [33], in good agreement with the findings of a previous local density approximation study [34]. The corresponding AFM configuration is energetically more stable than the FM configuration [33], consistent with the experimental situation [2, 6, 7, 8, 5]. Our calculated value of the Cr atomic spin moment of  $2.79 \mu_B$  for bilayer and monolayer  $\text{CrI}_3$  also closely corresponds to the experimental values [35, 36], and the monolayer magnetic anisotropy energy  $E_{\parallel} - E_{\perp}$  of 0.77 meV/Cr places the magnetization in the perpendicular direction, as found experimentally [35, 37], and in good agreement with the findings of previous theoretical studies (see Ref. [34] and references therein).

The band structure and the spin texture of the AFM bilayer are studied in the presence of an external electric field applied perpendicularly to the bilayer plane (positive  $z$  direction). The electric field is modeled with a sawlike potential along the  $z$  direction of the bilayer supercell. Dipole correction is applied to avoid spurious interactions between the periodic images of  $\text{CrI}_3$  along the direction of the external electric field [38, 39]. The layer-projected band structure and the corresponding weights of the states on each layer are obtained from the atomic pseudo-orbital projections of the states for the atoms in the layer.

Fig. 1 shows the side and top views of the  $\text{CrI}_3$  bilayer in the AFM configuration; the arrows denote the magnetic

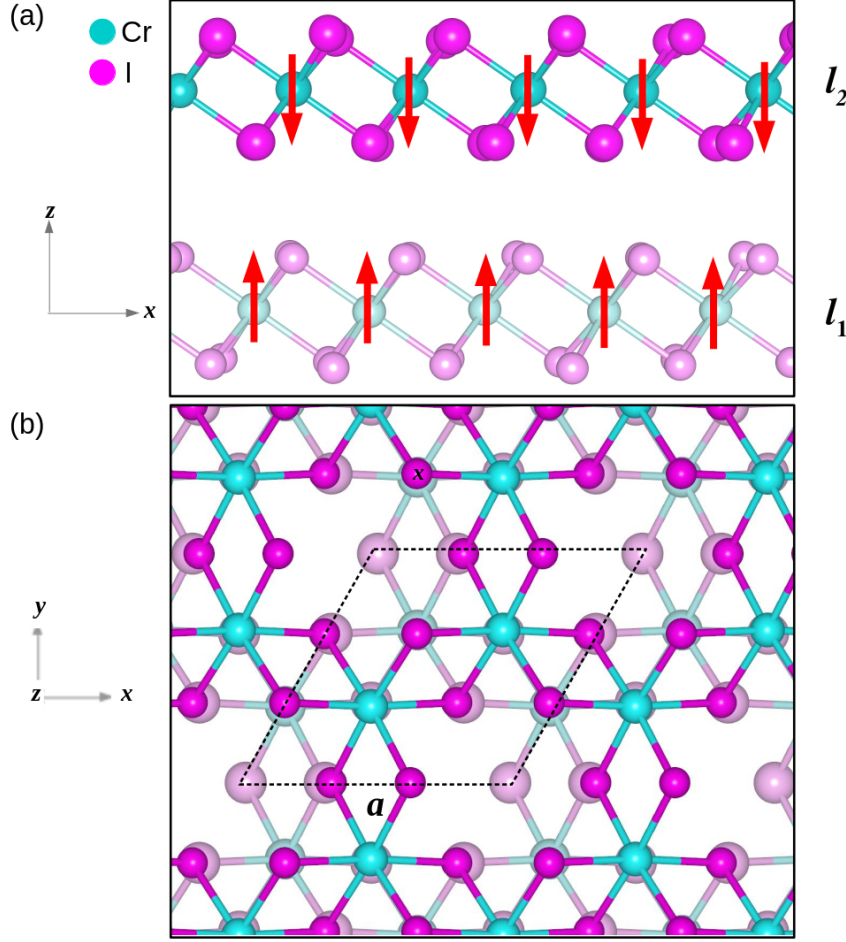


**Figure 1:** (a) Side view of the atomic structure of the antiferromagnetic CrI<sub>3</sub> bilayer with monoclinic layer stacking. In each CrI<sub>3</sub> monolayer, the plane of Cr atoms is sandwiched between two I atomic planes. The turquoise and magenta spheres represent the Cr and I atoms, respectively. The magnetic moments on the Cr atoms are denoted by the red arrows, while  $l_1$  and  $l_2$  stand for the two layers. (b) Top view of the CrI<sub>3</sub> bilayer, where the dashed black lines show the unit cell and  $a$  is the lattice parameter.

ordering on the two layers,  $l_1$  and  $l_2$ . The corresponding magnetic point group is  $C_{2h}$  ( $C_2$ ), with the following four symmetry operations: (i) identity E; (ii) 180° rotation about the  $y$  axis  $R_y[180^\circ]$ ; (iii) inversion combined with time reversal I·T; and  $x$ - $z$  mirror-plane reflection combined with time reversal  $M_{xz}$ ·T. The presence of the I·T symmetry implies that all bands of the pristine AFM bilayer are doubly degenerate (or multiples of that at some  $\mathbf{k}$  points); the pristine band structure is presented in Ref. [33]. The presence of the electric field breaks the I·T symmetry and lifts that degeneracy (and also breaks the  $R_y[180^\circ]$  symmetry).

We obtain the spin texture of the band states in  $\mathbf{k}$ -space by calculating the expectation values of the spin operators  $\frac{1}{2}\hat{\sigma}_\alpha$ ,  $\alpha = x, y, z$ , where  $\hat{\sigma}_\alpha$  are the Pauli matrices. The spin components corresponding to the  $i$ th energy spinor eigenfunction,  $\Psi_{i,\mathbf{k}}(\mathbf{r})$ , are obtained as

$$S_\alpha(\mathbf{k}) = \frac{1}{2} \frac{\langle \Psi_{i,\mathbf{k}} | \hat{\sigma}_\alpha | \Psi_{i,\mathbf{k}} \rangle}{\langle \Psi_{i,\mathbf{k}} | \Psi_{i,\mathbf{k}} \rangle}.$$

The particular calculation procedure to obtain the spin textures is given in the supplementary material.

We also examine the magnetization density,  $\mathbf{m}(\mathbf{r})$ , of some of the band states at selected  $\mathbf{k}$  points. The magnetization density components are evaluated as  $m_\alpha(\mathbf{r}) = \mu_B \Psi_{i,\mathbf{k}}^\dagger(\mathbf{r}) \hat{\sigma}_\alpha \Psi_{i,\mathbf{k}}(\mathbf{r})$ , where  $\mu_B$  is the Bohr magneton. When the states in the band are degenerate, as is the case in the AFM bilayer without an electric field, we evaluate the magnetization density components by summing over the degenerate states:

$$m_\alpha(\mathbf{r}) = \mu_B \sum_{i \in \text{band } n} \Psi_{i,\mathbf{k}}^+(\mathbf{r}) \hat{\sigma}_\alpha \Psi_{i,\mathbf{k}}(\mathbf{r}).$$

### 3. Results and discussion

In Fig. 2, we show the planar average of the magnetization density components  $m_x(z)$ ,  $m_y(z)$ , and  $m_z(z)$  for the highest valence band of the pristine AFM bilayer at two  $\mathbf{k}$  points, chosen at similar distances from the BZ center along the  $k_y$  axis [Fig. 2(a)] and along the  $k_x$  axis [Fig. 2(b)]. The magnetization density was obtained as the sum of the magnetization densities of the two degenerate states of the band at those  $\mathbf{k}$  points.

Apart from the  $m_z$  component parallel to the Cr-layer spin, which is virtually the same for the two  $\mathbf{k}$  points, we observe the presence of an in-plane magnetization-density component that strongly depends on the direction and length of the  $\mathbf{k}$  wavevector. The amplitude of this in-plane magnetization-density component is about one tenth that of the  $m_z$  component. For the  $\mathbf{k}$  point along the  $k_y$  axis,  $\mathbf{k} = (0, 0.15) \times 2\pi/a$ , in Fig. 2(a),  $m_x$  is significant and displays identical magnetization of opposite sign on the two layers of the bilayer,  $l_1$  and  $l_2$ , while  $m_y$  remains zero on both layers. The  $m_z$  component also changes sign on the two layers, following the sign of the Cr spins on the two layers. For the  $\mathbf{k}$  point along the  $k_x$  axis, in Fig. 2(b),  $m_y$  is also significant and inverts its sign from  $l_1$  to  $l_2$ , while keeping the same amplitude. In this case, the  $m_x$  component is not vanishing, but is of much smaller magnitude than the  $m_y$  component.

Thus, in both cases the magnetization-density component parallel to the  $\mathbf{k}$  vector is either zero ( $m_y$  in Fig. 2(a)) or much smaller than the in-plane tangential component ( $m_x$  in Fig. 2(b) is one order of magnitude smaller than  $m_y$ ). The behavior of the in-plane tangential magnetization-density components for both wavevectors is fully consistent with the tangential spin texture produced by the Rashba effect for electric field  $\mathbf{E}$  perpendicular to the layer, and corresponding effective magnetic field  $\mathbf{B}_{\text{eff}} \sim \mathbf{k} \times \mathbf{E}$ . In the AFM  $\text{CrI}_3$  bilayer, each layer feels an electric field originating from the presence of the other layer. The fields acting on the two layers are oppositely oriented (we estimate the strength of this intrinsic electric field to be on the order of  $0.1 \text{ V/\AA}$  at each layer; see the supplementary material). This creates tangential Rashba in-plane spin textures of opposite sign on the two layers.

For  $\mathbf{k}$  along the  $k_x$  axis, there is also a very small radial  $m_x$  magnetization-density component present on each layer. This originates in the local chirality of the FM monolayer (i.e., its lack of horizontal mirror-reflection symmetry), an effect discussed in detail in Ref. [40] for the FM bilayer. In the latter case, apart from this local chirality, the FM bilayer is also globally chiral (unlike the AFM bilayer), which results in dominant radial components along the  $k_x$  axis and equivalent directions of the FM bilayer [40]. For the AFM bilayer, the simultaneous tangential behavior and opposite signs of the magnetization-density components for the two layers at the two  $\mathbf{k}$  points (and also observed at other  $\mathbf{k}$  points) suggest a layer locking and spatial segregation of the degenerate states of the upper valence band with opposite helicities of the in-plane spin texture in the two layers.

To confirm the layer segregation of the states with opposite in-plane-canted spins, we applied a small electric field,  $E_{\text{ext}} = 0.05 \text{ V/\AA}$ , along the  $z$  direction of the unit cell, and evaluated the corresponding layer-projected band structure and corresponding layer-weighted spin texture. The electric field places each of the bilayer's layers at a different potential and thus splits the AFM degenerate energy levels according to the state's localization on  $l_1$  and  $l_2$ . The effect of this electric field on the  $\text{CrI}_3$  bilayer band structure is shown in Fig. 3. There, we also display the weight of every state on  $l_1$ . Importantly, the highest valence band is uniformly split nearly throughout the BZ, with a weight of the lower (upper) split state of more than 90% (less than 8%) on  $l_1$ . In other words, the two states belonging to the highest band are layer-separated: one is segregated on  $l_1$  and the other is segregated on  $l_2$ . It is important to underline that the electric field separates the states only in energy, while the spatial layer segregation of the states is a property of the pristine system. The only exceptions from the spatial segregation of the two highest states are around the special  $\mathbf{k}$  points  $K$  and  $K'$ , at which each state has a noticeable weight on both  $l_1$  and  $l_2$ . The highest valence states at the  $K$  and  $K'$  points are rather special already in the monolayer (where the states are degenerate; see the Appendix), and upon creation of the AFM bilayer, they interact, hybridizing and creating an energy splitting. To a smaller extent, also around  $\Gamma$ , the two highest valence states (especially the second-highest valence state), in Fig. 3, are not completely layer-locked. This can be similarly understood on the basis of the monolayer band structure (Fig. A1 in the Appendix); there, at the  $\Gamma$  point, the states of the two highest valence bands are particularly close in energy and tend to exhibit increased hybridization upon formation of the AFM bilayer. In Fig. 3, we can see that the other bands, both conduction and valence bands, are not uniformly split in general and that many are characterized by similar weights on the two layers. The upper valence band of the pristine AFM  $\text{CrI}_3$  bilayer [33] has the particular property of being separated in energy from the other bands. This separation somewhat decreases when the band splits as a result of the application

of  $E_{\text{ext}}$ . In Fig. 3, we can see that states that are closer in energy at a given  $\mathbf{k}$  point tend to display increased shared weight on the two layers of the bilayer, as is the case for the second and third valence states at  $K$ ,  $K'$ , and  $\Gamma$ .

In Fig. 4, we display the calculated in-plane spin texture for the two highest valence states, split upon the action of  $E_{\text{ext}}$ . We also show in Fig. 4 the isovalue color map of the perpendicular spin component  $S_z$ . As discussed above and based on Fig. 3, the spin textures in Fig. 4 also correspond to the layer-resolved spin textures (save for the states at  $K$ ,  $K'$ , and  $\Gamma$ ); the first split state represents the spin texture on  $l_2$  and the second split state represents the spin texture on  $l_1$ . For the first state  $S_z$  is always negative, and for the other state it is mostly positive. It can be seen immediately that the helicities of the in-plane spin texture on the two layers are opposite, as we expected on the basis of Fig. 2, and each of the layers is fully covered by only one of the two highest states. This confirms our deduction from Fig. 2 that the AFM  $\text{CrI}_3$  bilayer is indeed characterized by a Rashba-type in-plane spin texture in which the two highest valence states with opposite in-plane helicity are layer-locked with nearly full spatial segregation of the wavefunctions on the two layers. The in-plane spins have the largest magnitude at a radius of approximately  $0.15 \times 2\pi/a$  around the  $\Gamma$  point. They also have a relatively large amplitude around the  $M$  point along the  $K$ - $M$ - $K'$  line and around the  $M'$  point along the  $M'$ - $K'$  line. On the basis of the amplitude of the in-plane spin around  $\Gamma$  in Fig. 4, the Rashba coefficient for the upper valence band of the AFM bilayer is estimated to be  $0.6 \text{ eV \AA}$  (see the supplementary material).

It can be seen in Fig. 4 that in the parts of the BZ where the in-plane components are the strongest (in particular the ring region around the  $\Gamma$  point with radius of approximately  $0.15 \times 2\pi/a$ , and the regions around the  $M$  and  $M'$  points) the  $S_z$  component also has rather large values. The largest values of  $S_z$  are at  $\Gamma$  and at  $M'$  along the line  $M'$ - $K$ . At the same time, at the  $K$  and  $K'$  points, the  $S_z$  component virtually vanishes and even reverses sign in Fig. 4(b)—these are the same points where the states interact and lose the layer locking present everywhere else. We assign the appearance of  $S_z$  with reverse sign at the  $K$  and  $K'$  points in the second state to the presence of a very small amount of Cr  $d$  and I  $p$  states with opposite spin, observable already in the monolayer degenerate bands at  $K$  (see the Appendix). Thus, upon formation of the AFM bilayer, the monolayer states, each having both positive and negative  $S_z$  at  $K$  and  $K'$ , will interact between the layers and result in the mixed  $S_z$  character at each layer observed in Fig. 4 at  $K$  and  $K'$ . More details are given in the Appendix, also for the  $\Gamma$  point.

$E_{\text{ext}} = 0.05 \text{ V/\AA}$  is small enough to induce a linear splitting of the two states in the highest valence band and a first-order effect in  $E_{\text{ext}}$  on the spin texture. In the limit of vanishing  $E_{\text{ext}}$ , the in-plane spin textures of the two states have exactly the same magnitudes and opposite chiralities. The application of the electric field along the positive  $z$  direction slightly increases the amplitude of the in-plane spin component for the second valence state, while there is a small reduction of the in-plane spin component for the first valence state. For example, with  $E_{\text{ext}} = 0.05 \text{ V/\AA}$ , the largest amplitude of the in-plane spin increases (decreases) by  $0.004$  for the second (first) state with respect to its average of  $0.038$  for the two states. The difference in the strength of the in-plane spin components increases as  $E_{\text{ext}}$  increases. It could be envisioned that the electric field could be used to tune the relative strength of the in-plane spin texture of the two layers/states for the bands well separated in energy. The in-plane spin textures with  $E_{\text{ext}} = 0.1 \text{ V/\AA}$  and the corresponding band structure are reported in the supplementary material. For zero and small  $E_{\text{ext}}$ , the contribution to the spin texture of the two layers cancels in the band, while in the presence of a large external electric field, there is a nonvanishing overall spin texture.

We have shown that there is a pronounced layer locking of the in-plane-canted spin for the two highest valence states in AFM bilayer  $\text{CrI}_3$ . This layer locking without the typical Rashba energy splitting of the degenerate states has some resemblance to the mechanism of the “hidden Rashba spin-orbit splitting” (R-2) in centrosymmetric nonmagnetic crystals [24, 23], although in our case there is no (hidden) Rashba energy splitting between the two doubly degenerate bands interacting via the Rashba term (see the supplementary material). In nonmagnetic centrosymmetric crystals, all bands must be at least doubly degenerate, and global inversion symmetry (I) does not allow Rashba splitting into singly degenerate bands of opposite spin polarization. However, the presence of local asymmetry in the individual spatial I-partner sectors does permit the R-2 effect (with splitting into doubly degenerate bands) when the doubly degenerate states with opposite spin on the different sectors are prevented from mixing by a mechanism such as symmetry-enforced wavefunction segregation in nonsymmorphic crystals [24]. In the AFM bilayer, neither time-reversal symmetry nor inversion symmetry is present. All bands must, however, be doubly degenerate because of the presence of the symmetry operation I-T, and (although separated in energy) such bands interact via the Rashba term, as local asymmetry is also present in the individual I-T-partner sectors. The resulting two degenerate wavefunctions of the highest valence band are almost completely spatially segregated on the two layers (except near the BZ edge around the  $K$  and  $K'$  points, and at  $\Gamma$ )—see Fig. S3 in the supplementary material. In the R-2 effect, the segregation is not always complete, and when it is complete (in nonsymmorphic crystals), it occurs only along the high-symmetry direction in the BZ, where



the symmetry enforcing the wavefunction segregation is present [24]. In the AFM bilayer, an effect similar to (but not prohibitive for the mixing) that of the nonsymmorphic symmetries is produced by the layered AFM order with a perpendicular easy axis that naturally segregates the wavefunctions on the two layers. However, in our case, at the  $\mathbf{k}$  points where already in the FM monolayer two states are degenerate or quasi-degenerate, a complete spatial segregation in the AFM bilayer does not occur (see Figs. S5 and S6 in the supplementary material). Thus, we conclude that for a successful spatial wavefunction segregation of the two degenerate states of a van der Waals AFM bilayer band, it is crucial that the relevant monolayer states as well as the AFM band in question remain well separated in energy from the other bands.

#### 4. Conclusions

We have studied the spin texture in momentum space of the highest valence band of the AFM  $\text{CrI}_3$  bilayer characterized by the perpendicular easy axis. We found that it displays a Rashba spin texture with opposite sign of the in-plane spins on the two layers. In this case, the Rashba effect is not accompanied by an energy splitting of the degenerate bands. We applied a small electric field perpendicular to the bilayer that splits the degenerate states according to their layer localization. We observed a layer segregation of the states over nearly the whole BZ, each state belonging to only one of the two layers. At the high-symmetry points  $K$  and  $K'$ , and to a lesser extent at  $\Gamma$ , the segregation is destroyed by band interactions originating from degeneracies or near-degeneracies present in the  $\text{CrI}_3$ -monolayer band structure at those points. We compared the Rashba effect and layer locking of the in-plane-canted spin in the AFM  $\text{CrI}_3$  bilayer with the R-2 effect and the hidden spin polarization in nonmagnetic centrosymmetric crystals. Although in both cases the bands must remain doubly degenerate and the Rashba effect is enabled by the local asymmetry in the individual spatial inversion-related sectors, the segregation mechanisms differ in the two cases. We conclude that, while the layered AFM coupling makes the spatial segregation possible, the necessary condition is the separation in energy of the band in question.

We expect that a similar effect should be observed in other van der Waals AFM bilayers featuring a perpendicular easy axis, strong spin-orbit coupling, and a band isolated in energy. In all such systems, the relative strength of the in-plane canting of the spins of the two states/layers could also be tuned by the application of an external electric field.

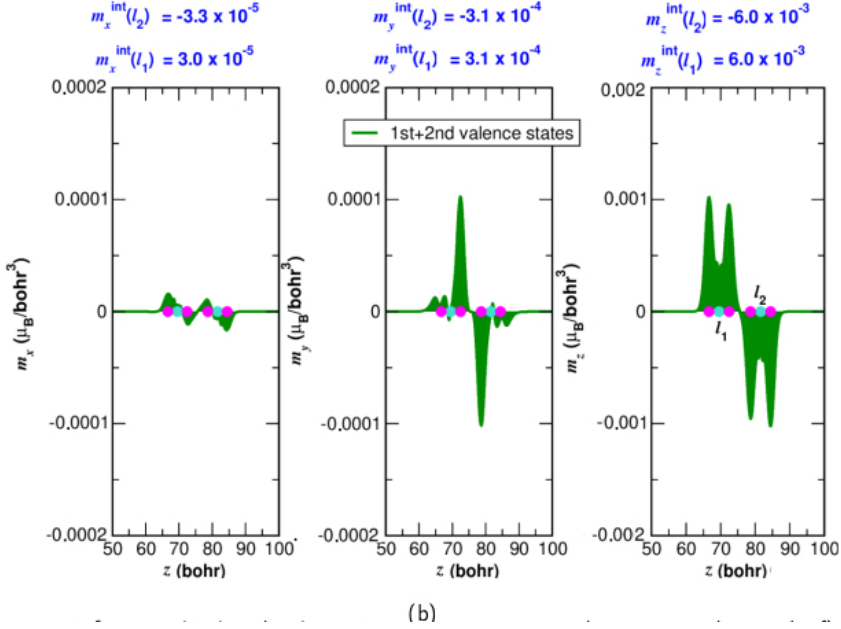
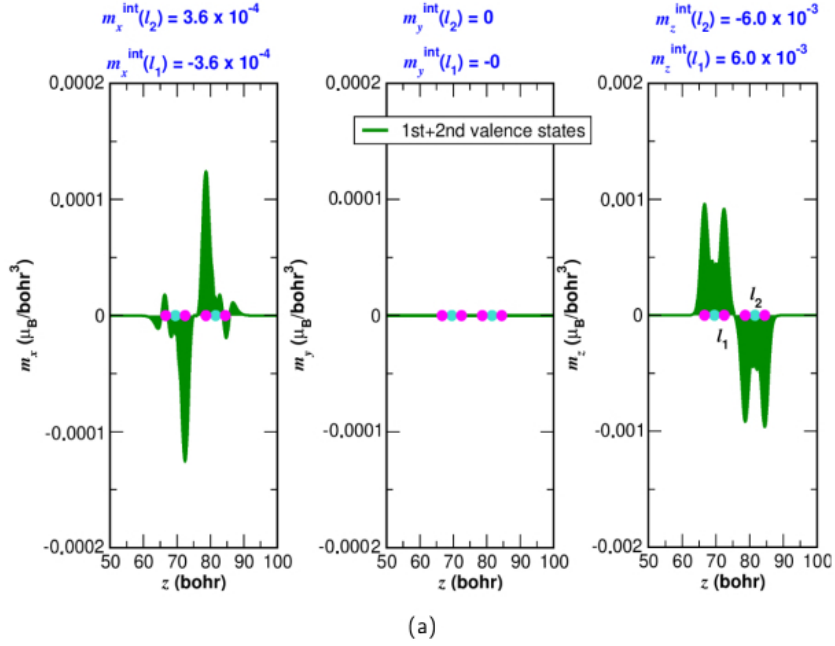


**Figure 2:** Planar average of magnetization-density components  $m_x$ ,  $m_y$ , and  $m_z$  summed over the first and second (the two highest) valence states of the pristine  $\text{CrI}_3$  bilayer in the antiferromagnetic configuration at (a)  $\mathbf{k} = (0, 0.15) \times 2\pi/a$  and (b)  $\mathbf{k} = (0.13, 0) \times 2\pi/a$ . The turquoise and magenta circles show the positions of Cr and I atoms, respectively, along the  $z$  direction of the supercell, and  $l_1$  and  $l_2$  denote the  $\text{CrI}_3$  layers in the bilayer. These two states contribute to form the highest valence band of the antiferromagnetic bilayer.  $m_i^{\text{int}}(l_1)$  and  $m_i^{\text{int}}(l_2)$ ,  $i = x, y, z$ , are obtained by integrating  $m_i$  on  $l_1$  and  $l_2$ , respectively, and are given in the unit of  $\mu_B/\text{bohr}^2$ .

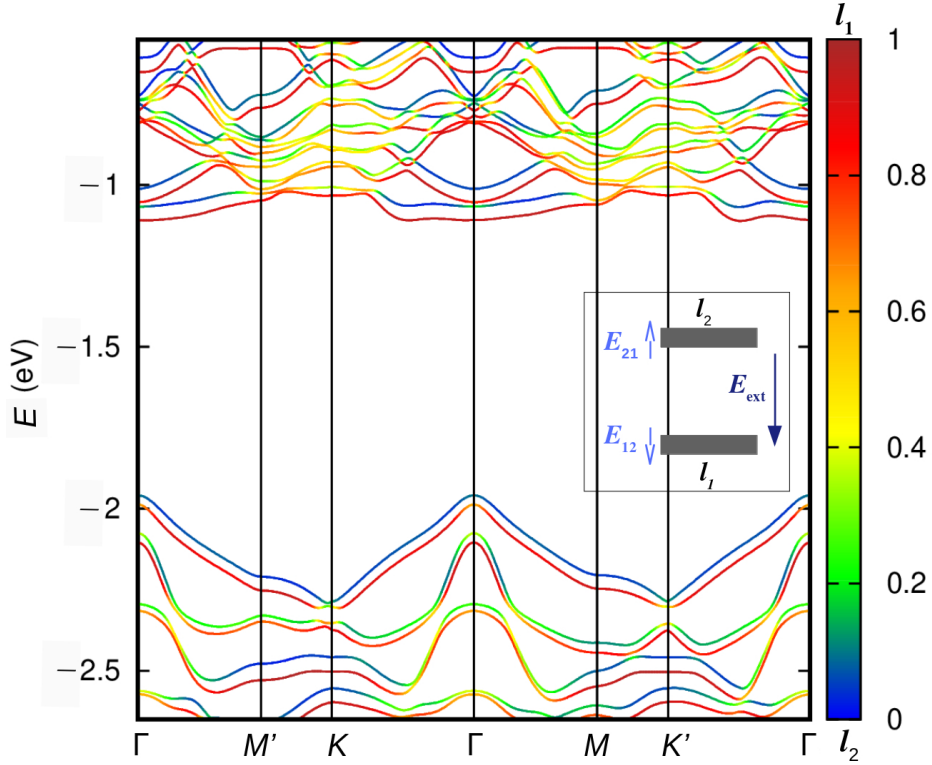


**Figure 3:** Band structure of the antiferromagnetic  $\text{CrI}_3$  bilayer in the presence of an external electric field,  $E_{\text{ext}} = 0.05 \text{ V/\AA}$ , applied along the out-of-plane direction of the  $\text{CrI}_3$  bilayer. Also shown is the color-coded weight of the states on layer 1 ( $l_1$ ) of the antiferromagnetic bilayer. The energy window includes the highest valence bands and the lowest conduction bands. The inset presents a schematic side view of the bilayer unit cell with the two monolayers  $l_1$  and  $l_2$ , where the light blue arrows denote the local internal electric fields  $E_{12}$  and  $E_{21}$  present in the bilayer and the dark blue arrow denotes the external electric field  $E_{\text{ext}}$ .



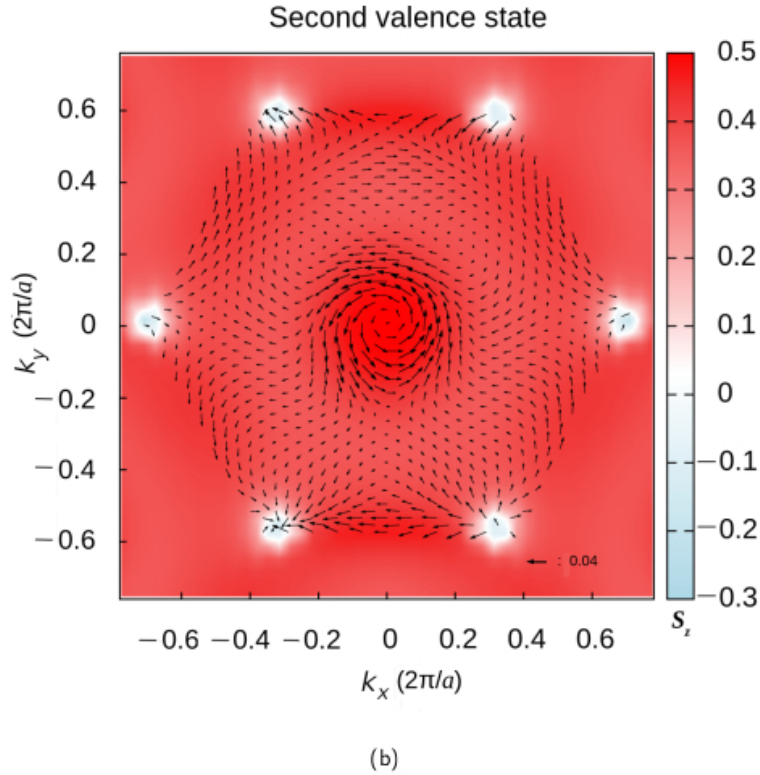
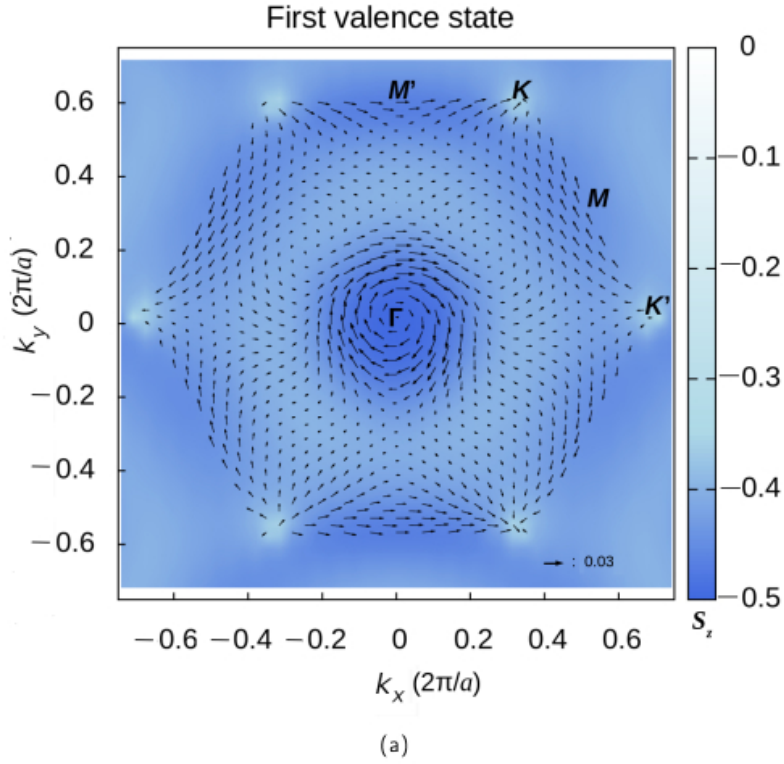


**Figure 4:** Spin-texture plots for (a) the highest and (b) the second-highest valence states in the Brillouin zone of the antiferromagnetic  $\text{CrI}_3$  bilayer in the presence of an electric field of  $0.05 \text{ V/\AA}$  applied perpendicularly to the bilayer. Each of the states is layer-locked on one layer of the bilayer (see also Fig. 3), the first state on  $l_2$  and the second on  $l_1$ . The in-plane spin components are represented by vectors and the perpendicular spin component is represented by the color scheme at the right of the plots. The reference value of the magnitude of the in-plane spin component is shown at the bottom of the plots.

## A. Appendix

In Figs. 3 and 4 we see that the layer locking of the two highest valence states shows some anomalies at the  $K$  and  $K'$  points, and to some extent also at  $\Gamma$ . This can be understood on the basis of the band structure of the pristine  $\text{CrI}_3$  monolayer in the FM configuration, which is given in Fig. A1. There, we also show the  $S_z$  projection on the energy bands. We see that the highest and second-highest valence states are degenerate at  $K$  and that they are very close in energy at  $\Gamma$ .  $S_z$  has the same sign for the first and second valence states at  $K$ , while at  $\Gamma$  the two states have opposite signs. The whole highest valence band is of roughly the same  $S_z$  (although it is somewhat reduced near  $K$ ).

The band structure of the weakly interacting bilayer with the AFM arrangement of layers can be viewed as a superposition of the  $S_z$ -projected band structure (in Fig. 3) and its time reversal ( $-S_z$ -projected band structure) with some further modulation of the band-structure dispersion due to the weak interlayer interactions. Indeed, the AFM  $\text{CrI}_3$  bilayer [33] has dispersions in the BZ for the highest valence states rather similar to those of the FM monolayer from Fig. A1. The main difference is the increase in energy of the first band around the  $\Gamma$  point and removal of the band crossing at  $K$  and  $K'$  in the bilayer case due to the interaction between degenerate states of the two layers.

It is thus expected that the character of the FM monolayer states at a given  $\mathbf{k}$  point will determine to a good measure the character of the bilayer states formed from those monolayers. The highest valence state of the  $\text{CrI}_3$  monolayer will form the first valence band of the AFM bilayer, with twofold degeneracy coming from the two layers with opposite spins. Interestingly, the band crossing at  $K$  of the two highest valence bands in the monolayer is nontrivial, as the highest valence band has a Chern number of 2 and the second-highest valence band near  $K$  is characterized by a Chern number of  $-2$  [41]. The 3D probability density of the monolayer's two highest states at  $K$  (see Fig. S6 in the supplementary material) shows that these states have localized density on different Cr atoms. The mean  $S_z$  for the degenerate states at  $K$  in the monolayer is only approximately 0.34. This makes it possible for the states of the two layers with opposite magnetization to hybridize upon formation of the bilayer, creating an energy splitting in the band structure of the bilayer.

At the  $\Gamma$  point, the two highest valence states of the monolayer are of opposite spin and rather close in energy. This allows some interactions between the two states on the different layers, upon formation of the AFM bilayer. In this case, however, because of the energy difference, each state of the monolayer only weakly hybridizes with the state of the other layer.

## Declaration of competing interest

The authors declare that they have no known competing financial interests or personal relationships that could have appeared to influence the work reported in this article.

## Data availability

The data that support the findings of this study are available from the corresponding author upon reasonable request.

## References

- [1] Cheng Gong, Lin Li, Zhenglu Li, Huiwen Ji, Alex Stern, Yang Xia, Ting Cao, Wei Bao, Chenzhe Wang, Yuan Wang, Z. Q. Qiu, R. J. Cava, Steven G. Louie, Jing Xia, and Xiang Zhang. Discovery of intrinsic ferromagnetism in two-dimensional van der Waals crystals. *Nature*, 546: 265–269, 2017.
- [2] Bevin Huang, Genevieve Clark, Efrén Navarro-Moratalla, Dahlia R. Klein, Ran Cheng, Kyle L. Seyler, Ding Zhong, Emma Schmidgall, Michael A. McGuire, David H. Cobden, Wang Yao, Di Xiao, Pablo Jarillo-Herrero, and Xiaodong Xu. Layer-dependent ferromagnetism in a van der Waals crystal down to the monolayer limit. *Nature*, 546(11):270–273, 2017.
- [3] Kenneth S. Burch, David Mandrus, and Je-Geun Park. Magnetism in two-dimensional van der Waals materials. *Nature*, 563:47–52, 2018.
- [4] Xiaoyang Lin, Wei Yang, Kang L. Wang, and Weisheng Zhao. Two-dimensional spintronics for low-power electronics. *Nat. Electron.*, 2:274, 2019.
- [5] Bevin Huang, Genevieve Clark, Dahlia R. Klein, David MacNeill, Efrén Navarro-Moratalla, Kyle L. Seyler, Nathan Wilson, Michael A. McGuire, David H. Cobden, Di Xiao, Wang Yao, Pablo Jarillo-Herrero, and Xiaodong Xu. Electrical control of 2D magnetism in bilayer  $\text{CrI}_3$ . *Nat. Nanotechnol.*, 13:544–548, 2018.
- [6] Nicolas Ubrig, Zhe Wang, Jérémie Teyssier, Takashi Taniguchi, Kenji Watanabe, Enrico Giannini, Alberto F. Morpurgo, and Marco Gibertini. Low-temperature monoclinic layer stacking in atomically thin  $\text{CrI}_3$  crystals. *2D Mater.*, 7(1):015007, 2019.
- [7] L. Thiel, Z. Wang, M. A. Tschudin, D. Rohner, I. Gutiérrez-Lezama, N. Ubrig, M. Gibertini, E. Giannini, A. F. Morpurgo, and P. Maletinsky. Probing magnetism in 2D materials at the nanoscale with single-spin microscopy. *Science*, 364(6444):973–976, 2019.

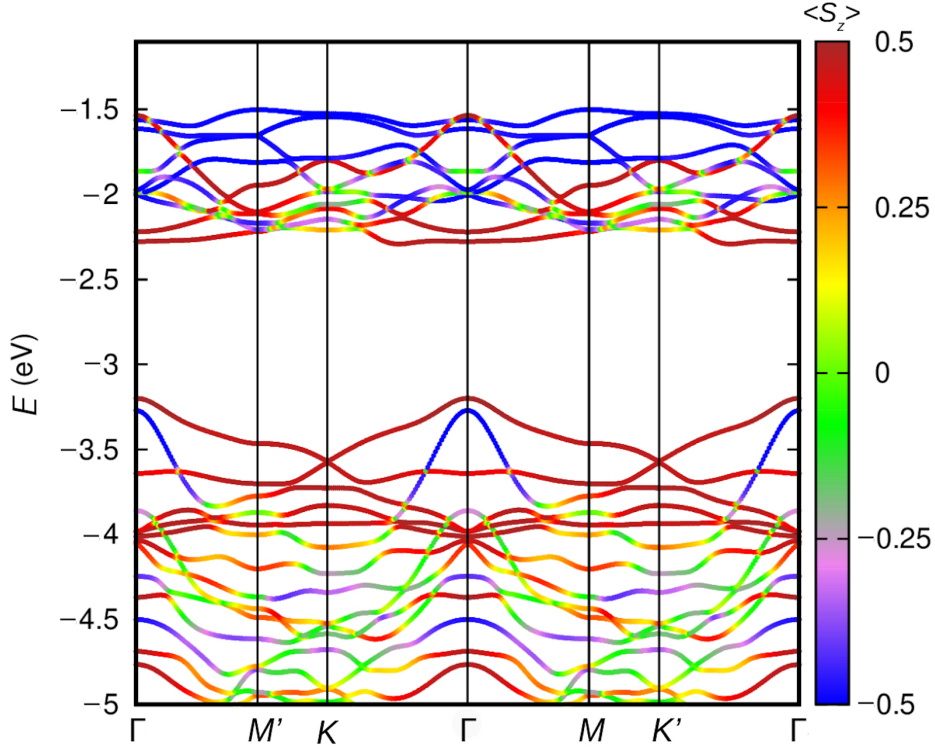


**Figure A1:** Spin-projected band structure of the ferromagnetic  $\text{CrI}_3$  monolayer. The projection of the mean  $S_z$  of the states is color-coded. The energy window includes the highest valence bands and lowest conduction bands.

- [8] Shengwei Jiang, Jie Shan, and Kin Fai Mak. Electric-field switching of two-dimensional van der Waals magnets. *Nat. Mater.*, 17:406–410, 2018.
- [9] T. Yungwirth, X. Marti, P. Wadley, and J. Wunderlich. Antiferromagnetic spintronics. *Nat. Nanotechnol.*, 11:231–241, 2016.
- [10] V. Baltz, A. Manchon, M. Tsoi, T. Moriyama, T. Ono, and Y. Tserkovnyak. Antiferromagnetic spintronics. *Rev. Mod. Phys.*, 90:015005, Feb 2018.
- [11] R. Lebrun, A. Ross, S. A. Bender, A. Qaiumzadeh, L. Baldrati, J. Cramer, A. Brataas, R. A. Duine, and M. Kläui. Tunable long-distance spin transport in a crystalline antiferromagnetic iron oxide. *Nature*, 561:222, 2018.
- [12] Shengwei Jiang, Hongchao Xie, Jie Shan, and Kin Fai Mak. Exchange magnetostriction in two-dimensional antiferromagnets. *Nat. Mater.*, 19:1295–1299, 2020.
- [13] Tiancheng Song, Zaiyao Fei, Matthew Yankowitz, Zhong Lin, Qianni Jiang, Kyle Hwangbo, Qi Zhang, Bosong Sun, Takashi Taniguchi, Kenji Watanabe, Michael A. McGuire, David Graf, Ting Cao, Jiun-Haw Chu, David H. Cobden, Cory R. Dean, Di Xiao, and Xiaodong Xu. Switching 2D magnetic states via pressure tuning of layer stacking. *Nat. Mater.*, 18:1298–1302, 2019.
- [14] D. R. Klein, D. MacNeill, J. L. Lado, D. Soriano, E. Navarro-Moratalla, K. Watanabe, T. Taniguchi, S. Manni, P. Canfield, J. Fernández-Rossier, and P. Jarillo-Herrero. Probing magnetism in 2D van der Waals crystalline insulators via electron tunneling. *Science*, 360(6394):1218–1222, 2018.
- [15] Tiancheng Song, Xinghan Cai, Matisse Wei-Yuan Tu, Xiaouo Zhang, Bevin Huang, Nathan P. Wilson, Kyle L. Seyler, Lin Zhu, Takashi Taniguchi, Kenji Watanabe, Michael A. McGuire, David H. Cobden, Di Xiao, Wang Yao, and Xiaodong Xu. Giant tunneling magnetoresistance in spin-filter van der Waals heterostructures. *Science*, 360(6394):1214–1218, 2018.
- [16] Hyun Ho Kim, Bowen Yang, Tarun Patel, Francois Sfigakis, Chenghe Li, Shangjie Tian, Hechang Lei, and Adam W. Tsen. One million percent tunnel magnetoresistance in a magnetic van der Waals heterostructure. *Nano Lett.*, 18(8):4885–4890, 2018.
- [17] Tula R. Paudel and Evgeny Y. Tsymbal. Spin filtering in  $\text{CrI}_3$  tunnel junctions. *ACS Appl. Mater. Interfaces*, 11:15781–15787, 2019.
- [18] Wei Yang, Yuan Cao, Jiangchao Han, Xiaoyang Lin, Xinhe Wang, Guodong Wei, Chen Lv, Arnaud Bournel, and Weisheng Zhao. Spin-filter induced large magnetoresistance in 2D van der Waals magnetic tunnel junctions. *Nanoscale*, 13:862–868, 2021.
- [19] Kapildeb Dolui, Marko D. Petrović, Klaus Zollner, Petr Plecháč, Jaroslav Fabian, and Branislav K. Nikolić. Proximity spin-orbit torque on a two-dimensional magnet within van der Waals heterostructure: current-driven antiferromagnet-to-ferromagnet reversible nonequilibrium phase transition in bilayer  $\text{CrI}_3$ . *Nano Lett.*, 20:2288–2295, 2020.
- [20] Zeyuan Sun, Yangfan Yi, Tiancheng Song, Genevieve Clark, Bevin Huang, Yuwei Shan, Shuang Wu, Di Huang, Chunlei Gao, Zhanghai Chen, Michael McGuire, Ting Cao, Di Xiao, Wei-Tao Liu, Wang Yao, Xiaodong Xu, and Shiwei Wu. Giant nonreciprocal second-harmonic

generation from antiferromagnetic bilayer  $\text{CrI}_3$ . *Nature*, 572:497–501, 2019.

- [21] Bevin Huang, John Cenker, Xiaou Zhang, Essance L. Ray, Tiancheng Song, Takashi Taniguchi, Kenji Watanabe, Michael A. McGuire, Di Xiao, and Xiaodong Xu. Tuning inelastic light scattering via symmetry control in the two-dimensional magnet  $\text{CrI}_3$ . *Nat. Nanotechnol.*, 15:212, 2020.
- [22] Ke Yang, Wentao Hu, Hua Wu, Myung-Hwan Whangbo, Paolo G. Radaelli, and Alessandro Stroppa. Magneto-optical kerr switching properties of  $(\text{CrI}_3)_2$  and  $(\text{CrBr}_3/\text{CrI}_3)$  bilayers  $\text{CrI}_3$ . *ACS Appl. Electron. Mater.*, 2:1373–1380, 2020.
- [23] Xiuwen Zhang, Qihang Liu, Jun-Wei Luo, Arthur J. Freeman, and Alex Zunger. Hidden spin polarization in inversion-symmetric bulk crystals. *Nat. Phys.*, 10:387–393, 2014.
- [24] Linding Yuan, Qihang Liu, Xiuwen Zhang, Jun-Wei Luo, Shu-Shen Li, and Alex Zunger. Uncovering and tailoring hidden Rashba spin–orbit splitting in centrosymmetric crystal. *Nat. Commun.*, 10:906, 2019.
- [25] J. Tu, X. B. Chen, X. Z. Ruan, Y. F. Zhao, H. F. Xu, Z. D. Chen, X. Q. Zhang, X. W. Zhang, J. Wu, L. He, Y. Zhang, R. Zhang, and Y. B. Xu. Direct observation of hidden spin polarization in  $2h\text{-MoTe}_2$ . *Phys. Rev. B*, 101:035102, 2020.
- [26] Cai Cheng, Jia-Tao Sun, Xiang-Rong Chen, and Sheng Meng. Hidden spin polarization in the 1t-phase layered transition-metal dichalcogenides  $\text{MX}_2$  ( $\text{M} = \text{Zr}, \text{Hf}; \text{X} = \text{S}, \text{Se}, \text{Te}$ ). *Sci. Bull.*, 63(2):85–91, 2018.
- [27] Wei Yao, Eryin Wang, Huaqing Huang, Ke Deng, Mingzhe Yan, Kenan Zhang, Koji Miyamoto, Taichi Okuda, Linfei Li, Yeliang Wang, Hongjun Gao, Chaoxing Liu, Wenhui Duan, and Shuyun Zhou. Direct observation of spin-layer locking by local Rashba effect in monolayer semiconducting  $\text{PtSe}_2$  film. *Nat. Commun.*, 8:14216, 2017.
- [28] Ke Zhang, Shixuan Zhao, Zhanyang Hao, Shiv Kumar, Eike F. Schwier, Yingjie Zhang, Hongyi Sun, Yuan Wang, Yujie Hao, Xiaoming Ma, Cai Liu, Le Wang, Xiaoxiao Wang, Koji Miyamoto, Taichi Okuda, Chang Liu, Jiawei Mei, Kenya Shimada, Chaoyu Chen, and Qihang Liu. Observation of spin-momentum-layer locking in a centrosymmetric crystal. *Phys. Rev. Lett.*, 127:126402, Sep 2021.
- [29] Feng Lou, Teng Gu, Junyi Ji, Junsheng Feng, Hongjun Xiang, and Alessandro Stroppa. Tunable spin textures in polar antiferromagnetic hybrid organic–inorganic perovskites by electric and magnetic fields. *npj Comput. Mater.*, 6:114, 2020.
- [30] Paolo Giannozzi, Stefano Baroni, Nicola Bonini, Matteo Calandra, Roberto Car, Carlo Cavazzoni, Davide Ceresoli, Guido L. Chiarotti, Matteo Cococcioni, Ismaila Dabo, Andrea Dal Corso, Stefano de Gironcoli, Stefano Fabris, Guido Fratesi, Ralph Gebauer, Uwe Gerstmann, Christos Gougousis, Anton Kokalj, Michele Lazzeri, Layla Martin-Samos, Nicola Marzari, Francesco Mauri, Riccardo Mazzarello, Stefano Paolini, Alfredo Pasquarello, Lorenzo Paulatto, Carlo Sbraccia, Sandro Scandolo, Gabriele Sclauzero, Ari P. Seitsonen, Alexander Smogunov, Paolo Umari, and Renata M. Wentzcovitch. QUANTUM ESPRESSO: a modular and open-source software project for quantum simulations of materials. *J. Condens. Matter Phys.*, 21(39):395502, 2009.
- [31] J. P. Perdew and Alex Zunger. Self-interaction correction to density-functional approximations for many-electron systems. *Phys. Rev. B*, 23:5048–5079, 1981.
- [32] P. E. Blöchl. Projector augmented-wave method. *Phys. Rev. B*, 50:17953–17979, 1994.
- [33] Sukanya Ghosh, Nataša Stojić, and Nadia Binggeli. Overcoming the asymmetry of the electron and hole doping for magnetic transitions in bilayer  $\text{CrI}_3$ . *Nanoscale*, 13:9391–9401, 2021.
- [34] A. M. León, J. W. González, J. Mejía-López, F. Crasto de Lima, and E. Suárez Morell. Strain-induced phase transition in  $\text{CrI}_3$  bilayers. *2D Mater.*, 7(3):035008, 2020.
- [35] Andreas Frisk, Liam B. Duffy, Shilei Zhang, Gerrit van der Laan, and Thorsten Hesjedal. Magnetic X-ray spectroscopy of two-dimensional  $\text{CrI}_3$  layers. *Mater. Lett.*, 232:5–7, 2018.
- [36] Michael A. McGuire, Hemant Dixit, Valentino R. Cooper, and Brian C. Sales. Coupling of crystal structure and magnetism in the layered, ferromagnetic insulator  $\text{CrI}_3$ . *Chem. Mater.*, 27(2):612–620, 2015.
- [37] Lebing Chen, Jae-Ho Chung, Tong Chen, Chunruo Duan, Astrid Schneidewind, Igor Radelytskyi, David J. Voneshen, Russell A. Ewings, Matthew B. Stone, Alexander I. Kolesnikov, Barry Winn, Songxue Chi, R. A. Mole, D. H. Yu, Bin Gao, and Pengcheng Dai. Magnetic anisotropy in ferromagnetic  $\text{CrI}_3$ . *Phys. Rev. B*, 101:134418, 2020.
- [38] Lennart Bengtsson. Dipole correction for surface supercell calculations. *Phys. Rev. B*, 59:12301–12304, 1999.
- [39] Sukanya Ghosh, Nataša Stojić, and Nadia Binggeli. Structural and magnetic response of  $\text{CrI}_3$  monolayer to electric field. *Physica B Condens. Matter*, 570:166–171, 2019.
- [40] Sukanya Ghosh, Nataša Stojić, and Nadia Binggeli. Chirality and Rashba-related effects in the spin texture of a 2D centro-symmetric ferro-magnet: the case of  $\text{CrI}_3$  bilayer. 2022. Preprint. arXiv:2206.10777 [cond-mat.mtrl-sci].
- [41] Santu Baidya, Jaeyun Yu, and Choong H. Kim. Tunable magnetic topological insulating phases in monolayer  $\text{CrI}_3$ . *Phys. Rev. B*, 98:155148, 2018.